

Where was the Iron Synthesized in Cassiopeia A?

Una Hwang¹ & J. Martin Laming²

ABSTRACT

We investigate the properties of Fe-rich knots on the east limb of the Cassiopeia A supernova remnant using observations with Chandra/ACIS and analysis methods developed in a companion paper. We use the fitted ionization age and electron temperature of the knots to constrain the ejecta density profile and the Lagrangian mass coordinates of the knots. Fe-rich knots which also have strong emission from Si, S, Ar, and Ca are clustered around mass coordinates $q \simeq 0.35 - 0.4$ in the shocked ejecta; for ejecta mass $2M_{\odot}$, this places the knots $0.7 - 0.8M_{\odot}$ out from the center (or $2 - 2.1M_{\odot}$, allowing for a $1.3M_{\odot}$ compact object). We also find an Fe clump that is evidently devoid of line emission from lower mass elements, as would be expected if it were the product of α -rich freeze out; the mass coordinate of this clump is similar to those of the other Fe knots.

Subject headings: none supplied

1. Introduction

Cassiopeia A is the only supernova remnant for which decays of the important radioactive nucleus ^{44}Ti have been confirmed by observation of γ ray line emission from both of its decay products, ^{44}Sc and ^{44}Ca (Iyudin et al. 1994, 1997; Vink et al. 2001; Vink & Laming 2003). The ^{44}Ti is almost uniquely produced in the explosive Si burning condition known as α -rich freeze out, wherein Si burns at high temperature and relatively low density. It takes place in the innermost ejecta and is highly sensitive to the explosion details and the

¹Goddard Space Flight Center and University of Maryland

hwang@orfeo.gsfc.nasa.gov

²Code 7674L, Naval Research Laboratory, Washington DC 20375

jlaming@ssd5.nrl.navy.mil

position of the mass cut for the formation of a neutron star or black hole. The location of α -rich freeze out is thus of great interest and importance to theoretical progress on the mechanisms by which core-collapse supernovae explode, but it is technically very difficult to directly image the hard X-rays or γ -rays from the ^{44}Ti decay at the necessary spatial resolution. An attractive alternative approach, recently proposed by Silver et al. (2001), is to search for Doppler structure in the ^{44}Sc emission lines at 67.9 and 78.4 keV using a very high spectral resolution calorimeter, but this also must await development of the required instrumentation.

A different approach explored in this paper depends on the nucleosynthesis signature of α -rich freeze out. The usual explosive Si burning produces mainly ^{56}Fe (originally as ^{56}Ni , which decays radioactively), along with Si, S, Ar, and Ca. Because α -rich freeze out happens very fast at low density and high temperature, the burning products are almost exclusively ^{56}Fe , apart from ^{44}Ti and a small amount of ^4He . The principal reason for this difference is that the low density suppresses the $3\alpha \rightarrow ^{12}\text{C}$ reaction, to shift the nuclear statistical equilibrium (or quasi-equilibrium) to heavier nuclei around the iron peak (Woosley & Hoffman 1991; Arnett 1996; The et al. 1998). Lighter nuclei, including ^{44}Ti , are formed in small amounts towards the end of the freeze out by α captures. The X-ray spectrum of a freeze out region should thus show emission lines only from Fe. It is our purpose in this paper to locate such Fe-rich region(s) in the extant Chandra observations of Cas A, and to characterize them in terms of their temperatures and ionization ages. By using a model for the supernova remnant hydrodynamics, we then place limits on the Lagrangian mass coordinates where such burning took place.

2. The Structure of Cassiopeia A

Early Chandra X-ray observations showed that the Fe emission in Cas A is associated with ejecta and is dominant to the east, in the faint region outside the bright ejecta shell. Since the Fe originates in the innermost ejecta, this suggests a large-scale turbulent overturn of the ejecta layers, either during or since the explosion (Hughes et al. 2000). In the northwest, the Fe emission coexists with emission from Si and other intermediate mass elements, at least in projection, but Doppler measurements made with XMM-Newton (Willingale et al. 2002) indicate larger line-of-sight velocities for Fe that imply that the Fe emitting region is actually kinematically and spatially distinct from that of other elements such as Si. Overturn of the X-ray emitting Fe layers thus appears to have occurred in the northwest as well as in the southeast, except that it is not viewed in a favorable orientation. Turbulent overturns are also inferred for the optically emitting S and Ar ejecta (Fesen 2001).

Typical X-ray surface brightness enhancements for the Fe features are only a factor of a few above their immediate surroundings. The Fe-rich knots will be shown here (also see Laming & Hwang 2003) to have higher characteristic ionization ages than the O/Si knots by factors of a few to ten,³ implying either a correspondingly higher density or an earlier shock time. Because knots and clouds with large density enhancements (or deficits) are subject to a number of hydrodynamical instabilities that act to destroy the knots within a few shock crossing timescales (Klein, McKee & Colella 1994; Klein et al. 2003; Wang & Chevalier 2001; Poludnenko, Frank, & Blackman 2001; McKee & Cowie 1975), such knots are not expected to survive longer than several tens of years after passage of the reverse shock. We believe that early shock times and very modest (or no) density enhancements are the most consistent explanation for the Fe knots that have survived to be observed today, and we make this assumption in what follows in this paper. We can thus account for the observed spectral characteristics of the knots, while allowing for their low surface brightness enhancements, and making it plausible for these shocked knots to exist at the present day. The low surface brightness enhancement that is observed for the Fe knots could be effected, not by increased density, but by the high emissivity of a Fe-rich plasma compared to a solar-abundance plasma at the same temperature and ionization age.

The survival of knotty ejecta in Cas A is supported by the hydrodynamical simulations of Kifonidis et al. (2000, 2003), who have modelled core collapse explosions in two dimensions with the aim of following the propagation of metal clumps within the ejecta. For a Type II explosion of a 15 M_{\odot} progenitor, they find that Rayleigh-Taylor instabilities at the interfaces between the Ni+Si and O layers and the O+C and He layers produce clumps of widely varying element compositions. As the explosion proceeds, however, the blast wave decelerates in the dense helium layer and generates a reverse shock that shreds and mixes the clumps. By a time 20,000 s after bounce, almost all the metals are completely mixed throughout the inner 3.4 M_{\odot} . The sole exceptions are those species like ^{44}Ti that are only synthesized in the innermost layers, and which remain correspondingly more localized. By contrast, a 15 M_{\odot} progenitor that loses its outer envelope to a stellar wind before exploding as a Type Ib supernova has a much weaker reverse shock. This reduces the effect of the mixing instabilities so that the metal clumps that are formed may survive and propagate further out into the ejecta. At time 3,000 s after bounce, ^{28}Si , ^{44}Ti and ^{56}Ni exist throughout the inner 2 M_{\odot} (of an explosion progenitor of 5.1 M_{\odot}).

There is little doubt that the explosion of Cas A was of Type Ib so that, based on the above, ejecta knots should have initially survived the mixing instabilities that operated

³The ionization age $n_e t$ is defined as the product of electron density and the time since the plasma was shock-heated.

during the explosion. For example, Laming & Hwang (2003) give various arguments to suggest that the progenitor’s main sequence mass was 20-25 M_{\odot} (at the lower end of the range of Wolf-Rayet masses), and that the progenitor possibly underwent a short phase as a WN star before exploding at 3-4 M_{\odot} . Similar inferences have been made based on studies of the optically emitting fast-moving knots (Fesen et al. 1988; Fesen 2001, and references therein). Indeed, there is substantial evidence to support a circumstellar environment for Cas A. Slow-moving, N-rich optically emitting knots are generally accepted to be relics of the progenitor’s mass loss, and a wind circumstellar density profile is far more viable than a constant density environment in the light of such observations as the relative radii of the reverse and forward shocks (Gotthelf et al. 2001), the X-ray expansion rate (DeLaney & Rudnick 2003), and also in terms of the implied ejecta mass and the production of nonthermal X-ray bremsstrahlung emission by electrons accelerated by lower hybrid waves (Laming 2001a,b; Vink & Laming 2003).

In a companion paper (Laming & Hwang 2003, Paper I), we use a new approach to make a quantitative analysis of the X-ray emitting ejecta of Cas A, specifically with regard to asymmetries in the ejecta and explosion. The method of Laming & Hwang (2003) makes the assumptions that Cas A is propagating into a circumstellar environment (i.e., the dependence of the density ρ on the radius r is $\rho \propto r^{-2}$) and that the spectra of individual knots can be modelled with a single temperature and ionization age. Arguments have just been presented for a circumstellar environment for Cas A. A single temperature and ionization age may plausibly be used to model the spectra of the knots because the knots have angular scales of $\sim 1''$ in the Chandra images, corresponding to $\sim 5 \times 10^{16}$ cm (at a distance of 3.4 kpc). A 1000 km/s reverse shock can traverse such a knot in just 20 years—a time period much shorter than the timescale for the dynamical evolution of the remnant.

The model of Laming & Hwang (2003) extends the analytical hydrodynamical description of remnant evolution of Truelove & McKee (1999) to a $\rho \propto r^{-2}$ circumstellar environment, and includes the basic relevant atomic and plasma physical processes: the time-dependent ionization balance in shock-heated gas, Coulomb heating of the electrons by the ions (i.e., no additional collective plasma heating is assumed), and radiative and adiabatic expansion losses. The ejecta themselves are assumed to have a power-law density distribution with a uniform density core. The shocked ejecta mass is taken to be 2 M_{\odot} , whereas the explosion energy and ambient density are adjusted. These models are used to predict the time-dependent behavior of the temperature and ionization age of the knots, which are then compared to the temperatures and ionization ages inferred for the ejecta knots from their Chandra X-ray spectra. This approach allows us to deduce the slope of the ejecta envelope in each of the azimuthal directions we examine; by forcing the models to share a common core ejecta density and fixing the forward shock radius in the models to match the observed

average X-ray radius, we may interpret the inferred variations in the ejecta envelope slope as due to variations in the locally deposited explosion energy. The variations we deduce are modest, at about a factor of two in energy, with shallower slopes (and higher inferred explosion energy) at the base of the ejecta jet in the northeast than in the east or northwest. A factor of two asymmetry is at the low end predicted by models, but at present, it is not possible on the basis of ejecta density and energy asymmetries alone to distinguish between the two basic mechanisms to produce explosion asymmetries, namely rotation of the progenitor or a jet-induced explosion (Fryer & Heger 2001; Fryer & Warren 2003; Khokhlov et al. 1999). Asymmetries of a comparable magnitude may also be produced by the instability that can arise in the standing accreting shocks of core-collapse supernovae as the injection of vorticity drives the rapid growth of turbulence behind the shock (Blondin, Mezzacappa & DeMarino 2002).

3. Data Reduction and Analysis

For the imaging analysis and most of the spectral analysis, we use the same January 2000 Chandra observation of Cas A with the Advanced CCD Imaging Spectrometer (ACIS) that is used and described by Laming & Hwang (2003). For one interesting and faint region, however, we also use data from a second epoch observation of Cas A taken two years after the first, in January 2002. Both observations are of 50 ks duration and were taken with the same instrument in the same configuration. The spectra from the two epochs are fitted jointly, rather than being added into a single spectrum, because of the time-varying response of the ACIS detector. These effects include time-dependent changes in the gain and resolution caused by charge-transfer inefficiency, and in particular, the temporally increasing absorption of soft X-rays (with energies below about 1 keV) by contaminants that build up on the detector surface. This detector absorption is modelled by ACISABS in the XSPEC X-ray spectral fitting package, with the number of days elapsed from launch to the observation date specified (198 days for the 2000 observation and 929 days for the 2002 observation).

3.1. Identification of Fe-rich Regions

In searching for regions dominated by Fe ejecta, we are aided by the combined spectral and imaging capabilities of the Chandra Observatory. X-ray images of Cas A in its prominent Fe K blend (energy ~ 6.7 keV) show that this emission is distributed in three primary regions—to the southeast, northwest, and west (Hwang, Holt, & Petre 2000; Willingale et al. 2002). The western region suffers from a higher interstellar column density that attenuates

the low energy X-ray emission, so that the Fe L emission (energies near 1 keV) is prominent only in the southeast and northwest. The southeast region is of particular interest in that the Fe emission here is located exterior to that of Si.

The left panel of Figure 1 shows the southeast region of Cas A. The blast-shocked material may be seen in places as faint, thin arcs at the outer boundary of the remnant, while the ejecta make up the bright irregular ring of emission. The faint, linear filaments of the ejecta “jet”, which are also seen optically, can be seen towards the top of the image. East of the bright ejecta ridge running southward from the jet, the fainter ejecta emission is largely Fe-rich. The Fe features have various morphologies ranging from compact knots to elongated knots, to relatively diffuse features.

Regions of the remnant that have strong line emission relative to the underlying continuum may be selected independently of surface brightness by forming an estimate of the line-to-continuum ratio at each position. For the Fe L blends, it is difficult to reliably subtract the true continuum, but in order to identify the Fe-richest regions, we have used spectral regions on either side of the L blend to make a rough estimate of the underlying continuum. The right panel of Figure 1 shows the Chandra image in the Fe L blends overlaid with smoothed contours showing the regions with prominent Fe L line-to-continuum ratios. It is seen that the strongest Fe line emission comes from a line of compact knots running due east at DEC $\sim 58^{\circ}46'40''$ as well as from diffuse regions of relatively low surface brightness about an arcminute to the south. These are thus our primary target regions to search for sites of α -rich freeze out. The spectral extraction regions (generally a few arcseconds in extent) are shown in the left panel of Figure 1.

The level of surface brightness contrast seen for the Fe and Si features is illustrated in Figure 2. The first panel shows a vertical cut through two representative Fe knots (numbered 13 and 14, starting with 10 closest to the center⁴). The knots are seen to sit on a shelf of emission that rises above the general background. The second panel shows a vertical cut through the larger diffuse Fe-rich cloud. It too sits on a shelf of even fainter emission, but the surface brightness contrasts are seen to be significantly lower than for the other Fe-rich knots. In comparison, typical Si-rich emission features are much brighter than either the background or the Fe-rich emission, as is seen in the remaining two panels of Figure 2.

⁴The radial series of knots is the extension eastward of the east series of knots studied in Laming & Hwang (2003); thus the numbering scheme here starts where that series left off at A10, increasing eastward to A17.

3.2. X-ray Spectral Analysis

We carried out spectral fits for the regions indicated in Figure 1 with a model characterized by a single temperature and single ionization age, wherein the lightest element included is O, and O provides the bulk of the continuum. This is consistent with the expectation that O is the primary constituent of the ejecta in Cas A, and follows the approach first adopted by Vink, Kaastra, & Bleeker (1996) for modelling the X-ray ejecta spectra with an O-rich plasma. The most prominent features in the spectra we consider are, however, from Fe. We also consider models where Si, rather than O, is the lightest element. The background spectrum is generally taken from positions well off the source. For the Si/Fe ejecta models, we also take a more localized background from low-surface brightness regions in the eastern part of the remnant near the Fe knots. The results of all these fits are summarized in Table 1, and the fits for a typical knot are shown in Figure 3.

For the Fe knots (A series), the fits using the standard off-source background are generally better with O ejecta than with Si ejecta. In both cases, the fitted ionization ages are $\sim 10^{11}$ cm⁻³s or higher, while the O continuum fits give temperatures that are higher by a few tens of percent. The use of a local background for the Si/Fe continuum fits naturally lowers the fit statistic per degree of freedom because the local background is less precisely determined than the standard background, but the actual fitted parameters are not much changed.

The spectrum of the local background and of the regions surrounding the compact Fe-rich knots do show enhanced emission from Fe, with fitted Fe/Si abundance ratios of roughly 1–1.5 times solar. These Fe/Si ratios are significantly higher than in the Si-rich knots studied by Laming & Hwang (2003)—which are nearly devoid of Fe—but not as high as in the compact Fe knots in Table 1; the fitted Fe/Si ratio increases for regions closer to the compact knots. The fitted ionization ages are several times 10^{10} to 10^{11} cm⁻³ s, which is within a factor of 2-3 of most of the ionization ages given in Table 1 for the compact knots.

The faint c6a region lying southward of the knots in the A series is the most interesting of the Fe-rich features. For this faint feature we show the fits using the local background only, as the off-source background gives statistically unacceptable fits. The spectrum is well-fitted with a model including only the elements Si and Fe (plus Ni), provided that the two elements can have different values of the ionization age. The temperature and ionization age for Fe are similar to those obtained for the Fe-rich knots in Table 1, while the Si ionization age is similar to that obtained in Laming & Hwang (2003) for the O/Si knots. We also performed a simultaneous fit of epoch 2000 and 2002 ACIS observations for this feature, allowing the two spectra to have different amounts of detector absorption according to their observation date. The parameters obtained are all very close to those obtained with the

epoch 2000 observation alone, although with slightly smaller error ranges. Both sets of fits for the c6a region are shown in Figure 4, and the results summarized in Table 2. The Si and Fe ionization ages are not consistent with each other in either of the fits; their equality can be excluded at higher than 99% confidence from the error contours shown in Figure 4 for the joint fit.

The line-to-continuum ratio images in Figure 1 show that the regions near c6a having very slight surface brightness enhancements over the background should have high Fe line strengths. We therefore extracted source and background spectra for this entire region by specifying appropriate surface brightness cuts on the slightly smoothed image. The resulting background-subtracted spectrum can be fitted with a single component model including only Si and Fe (and Ni), but does not necessarily require Si and Fe to have separate ionization ages. An enhancement of the Fe/Si abundance ratio at a level comparable to that found for the Fe knots is indicated. Thus, while this entire region is significantly Fe-enriched, on the whole it is not as pristine in Fe as is c6a. We have examined a number of other features in this region, and while many of them show Fe enrichments of the order of the Fe knots, we have so far identified no others where the Fe is as pure as in c6a.

The Fe-rich knots considered here have Fe/Si abundance ratios that are higher, generally by an order of magnitude or more, than the typical 0.25 ratio that is obtained through incomplete explosive Si-burning in a $20 M_{\odot}$ progenitor (see Table 2 in Thielemann et al. 1996). It is clearly indicated that some of the Fe is produced with complete Si exhaustion, as is already well-established, both by earlier X-ray spectral observations (Hughes et al. 2000) and by the confirmed detection of the decay products of ^{44}Ti , which is formed by α -rich freeze out (complete Si-burning that occurs at lower densities). The explicit identification of a possible pure cloud of Fe ejecta in region c6a suggests strongly that this may be one of the sites where α -rich freeze out occurred in Cas A.

The fitted ionization ages for the regions surrounding the A series of knots in the east are lower than, but of the same order of magnitude as that in the knots themselves. A density contrast of a similar amount (a factor of 2-3) may still exist without triggering the hydrodynamic instabilities in a manner that destroys the knots. Laming & Hwang (2003) demonstrate that the curves of T_e against $n_e t$ are essentially unchanged for such small degrees of clumping. The Fe/Si abundances of \sim solar for this region are also at least a factor of two lower than the average Fe/Si abundance in the compact knots. It seems reasonable to infer that the Fe in the gas surrounding the compact knots was stripped from Fe-rich knots that initially had higher density contrasts compared to their surroundings and therefore did not survive the action of instabilities. Another possible interpretation would be that the abundances surrounding the knots are the result of incomplete explosive Si burning,

compared with complete explosive Si burning in the compact knots themselves (see e.g. Thielemann et al. 1996).

4. Fe Ejecta Models and Discussion

In connection with Fe ejecta knots, it is also necessary to consider that ^{56}Fe is originally formed as ^{56}Ni , which decays radioactively. If the initially formed Ni clumps are sufficiently large, they will be opaque to the γ ray radiation produced by the decays, and thereby expand to form a hot, low-density Fe bubble. As the reverse shock traverses these bubbles, the resulting turbulence plays an important role in mixing the Fe ejecta into overlying ejecta layers (Li, McCray, & Sunyaev 1993), as well as causing filamentation in the overlying (Si-rich) ejecta (Blondin, Borkowski & Reynolds 2001). The Fe associated with the bubble effect should be characterized by diffuse morphologies and low ionization ages. The relative compactness of an Fe ejecta knot seen in the Type Ia (thermonuclear runaway) remnant of Tycho’s supernova, caused Wang & Chevalier (2001) to suggest that the Fe in question there is not ^{56}Fe , but rather ^{54}Fe , which is not formed by radioactive decays and is therefore not subject to the bubble effect. For core-collapse supernovae, and for Cas A in particular, this is a less satisfactory explanation because it is then difficult to produce a sufficient mass of ^{54}Fe , particularly if α -rich freeze out occurred during the explosion. The bubble mechanism has also been suggested to be connected with the ring-like filamentation seen in the optically emitting ejecta (Fesen 2001), and indeed may be responsible for the highly filamentary X-ray emission from Si as well. Presumably any Fe associated with the bubble effect is now too faint and underionized to be readily identifiable. On the other hand, if some of the ^{56}Ni clumps were sufficiently small at the outset, these could become optically thin to the γ -ray radiation sufficiently early on that the bubble effect would be minimized for these clumps. These are the Fe clumps that we see today.

We can demonstrate that these Fe clumps were indeed small enough to minimize the bubble effect. The observed clump diameters of about $3''$ give present day radii of 7.5×10^{16} cm at the 3.4 kpc distance of Cas A. Assuming that the radius increased proportionally to time, we get $r = 6 \times 10^{11} t_{\text{days}}$ cm for the radius of a $^{56}\text{Ni}/^{56}\text{Co}$ clump at time t_{days} days after the explosion. The clump electron density varies as t^{-3} until interaction with the reverse shock, so extrapolating our $n = 7$ model back in time gives an electron density in the range $n_e = (1.5 - 3) \times 10^{14}/t_{\text{days}}^3 \text{ cm}^{-3}$. The optical depth to the center of the clump is then (Li, McCray, & Sunyaev 1993)

$$\tau(t_{\text{days}}) \simeq \sigma n_e r \simeq (18 - 36) / t_{\text{days}}^2, \quad (1)$$

where $\sigma = 0.31\sigma_{\text{T}}$ for γ rays of energy about 1 MeV, and σ_{T} is the Thomson cross section.

Hence we estimate that these clumps became optically thin ($\tau \sim 1$) to their own γ rays about 5 days after explosion. This is significantly shorter than the ^{56}Ni and ^{56}Co lifetimes of 8.8 and 111.3 days, respectively, so most of the radioactive energy is deposited outside the clump. We therefore do not expect that the Fe knots we observe today have undergone any type of bubble expansion.

We pursue a more quantitative interpretation of the Fe knots in Cas A than has been previously attempted, by calculating the variation of the electron temperature T_e with ionization age $n_e t$ for a variety of ejecta density profiles, as described in Laming & Hwang (2003). We concentrate on models with an explosion energy of 2×10^{51} ergs, shocked ejecta mass $2M_\odot$, and circumstellar density $\rho r_b^2 = 14 \text{ pc}^2 \text{ cm}^{-3}$, with r_b the radius of the blast wave in pc. Laming & Hwang (2003) treated the case of pure O ejecta only; here we take compositions by mass of O:Si:Fe = 0.83:0.06:0.11 and Fe:Si = 0.9:0.1, which are approximately consistent with the spectral fits to the observed knots assuming an O-rich and Fe dominated composition for the continuum, respectively. These models are shown in Figures 5 and 6 as solid lines; the fit results are superposed as crosses for the “A” series of knots and, in Figure 6 only, as boxes for the diffuse Fe clouds, with the symbol size indicating the fit uncertainties in T_e and $n_e t$. Table 3 gives the ejecta mass coordinates inferred for each knot by matching the fitted value of $n_e t$ to the corresponding location in the ejecta for the hydrodynamic model. In this, we assume that the clumps have the same density as their surroundings, and infer electron densities of $10\text{-}50 \text{ cm}^{-3}$ for the clumps. If the knots are actually overdense, the $n_e t$ we fit would correspond to a later reverse shock passage and hence place the knots further in in the ejecta. We estimate that a factor of three overdensity would lead to an overestimate of q by around 0.06; a similar underdensity would place the knots further out in the ejecta, by a similar amount. Following reverse shock passage, our Lagrangian plasma parcel likely undergoes interactions with secondary shocks while the reverse shock is relatively nearby, leading in any case to uncertainties in q of a similar magnitude.

The mass of ^{56}Fe contributed by the various knots is computed from the fitted emission measure and element abundances of the knots in Table 3. Spherical geometries were assumed for the knots, and boxes for the diffuse features. The corresponding electron densities are also given in the table, and for comparison, the electron densities that are inferred from the models. The agreement between the observationally and theoretically inferred densities is generally within a factor of two, though it is somewhat worse for the larger East region. In any case, the observationally determined electron densities are systematically lower than the theoretically determined ones, which would seem to reinforce our assumption that the knots are not overdense.

According to the hydrodynamical model in Laming & Hwang (2003), the reverse shock

is currently at an ejecta mass coordinate $q = 0.1 - 0.14$ for $n = 9 - 7$ models respectively. Hence the inner 10% of ejecta, i.e. the inner $0.2 M_{\odot}$, has yet to encounter the reverse shock. Cas A is highly unlikely to have ejected more than $0.05 - 0.1 M_{\odot}$ of ^{56}Ni (which β decays to ^{56}Fe), so the reverse-shocked ^{56}Fe that we do see must have been mixed out into the envelope by Rayleigh-Taylor instabilities shortly after explosion. The estimated knot masses in Table 3 probably amount to a few percent of the total mass ejected, which is similar to the mass of ^{56}Ni inferred to have been mixed out into the envelope of SN 1987A (Pinto & Woosley 1988).

According to the mass coordinates we infer, the Fe clumps exist out to about 0.4 of the $2 M_{\odot}$ ejecta, or $0.8 M_{\odot}$. Adding $1.3 M_{\odot}$ for the mass of the compact object, we arrive at $0.8 + 1.3 = 2.1 M_{\odot}$ for the observed outer extent of Ni mixing. This places the knots at a mass coordinate corresponding to the (Ni+Si)/O interface in a star that is initially of about $20 M_{\odot}$ (Woosley & Weaver 1995). Though this is an appealing inference, it is necessary to account for possible selection effects that determine the visibility of the knots. In the case of an O-rich composition for the knots, this apparent outer extent appears to be a real outer extent (see Figure 5). We expect that if higher $n_{\text{Fe}}t$ knots exist now, we would be able to see them. For Fe-dominated composition, however, knots that encounter the reverse shock earlier than about 35 years after explosion (at ejecta mass coordinates $q_{\text{FeSi}} \gtrsim 0.45$) will have by now cooled by radiative losses to temperatures below detectability as X-ray knots. In this case, the observed outer extent could be limited by this selection effect. We also fail to detect Fe knots with $n_{\text{Fe}}t \lesssim 10^{11} \text{ cm}^{-3}\text{s}$, i.e. in the inner 0.3 of the ejecta, or interior to $1.9 M_{\odot}$, if the compact object is included. This might also be a selection effect caused by the rapid decrease in density as one move inwards into the ejecta. Fe that is deep in the ejecta may also be more likely to have created bubbles due to the radioactivity of its parent ^{56}Co nucleus, and so become even less dense than the O-rich ejecta that is assumed to surround it. The inferred mixing of the “c6a” and “east” regions out into regions that were originally O and are burnt to Si during the explosion, is also consistent with the inference that ^{44}Ca found in SiC X grains is a decay product of ^{44}Ti formed in core collapse supernovae (e.g. Clayton et al. 2002).

It appears that the O:Si:Fe composition we infer can only be achieved by mixing products of complete Si burning with the products of O burning (to get Fe:Si right), and it is unlikely that a “knot” would survive such mixing as a distinct object. More plausible is the pure Fe:Si composition, that requires no further mixing after Si burning. Consequently the selection effect due to the radiative cooling of Fe rich knots discussed above is probably operative, and more Fe may exist at lower temperatures further out in the ejecta of Cas A.

5. Conclusions

Using Chandra observations combined with new modelling techniques, we have constrained the ejecta density profiles and Lagrangian mass coordinates of some of the Fe-rich knots in the southeastern region of Cas A. This makes it possible for the first time to compare observations in a quantitative manner with explosion models, and allows tests of nucleosynthesis and Rayleigh-Taylor instability in core collapse supernova explosions. The inference is that Fe and Si in knots are relatively uncontaminated by lower Z elements, and that their inferred ejecta mass coordinates appear to be entirely consistent with the expected Rayleigh-Taylor turbulence in a Type Ib supernova. We have further identified a region of nearly pure Fe ejecta that is a promising candidate for a site of α -rich freeze out. Again it is mixed out by Rayleigh-Taylor turbulence, but as a site α -rich freeze out associated with ^{44}Ti production, its origin should have been closer to the center and the mass cut than those of the other Fe rich knots.

It is clearly desirable to make a complete census of the X-ray emitting Fe ejecta regions in Cas A and identify more regions that are highly enriched in Fe. For example, the ejected ^{44}Ti mass is estimated at $1.8 \times 10^{-4} M_{\odot}$ (Vink et al. 2001; Vink & Laming 2003), and 500-1000 times more ^{56}Ni by number is predicted globally from α -rich freeze out (Woosley & Hoffman 1991; Arnett 1996; Thielemann, Nomoto & Hashimoto 1996; The et al. 1998), so considerably more α -rich freeze out ashes should be present in Cas A to account for the ^{44}Ti emission than are inferred to be in regions “east” and “c6a”. In this work we have principally been limited by the statistical quality of the current Chandra data sets when extracting spectra from the smallest possible spatial regions. A considerably deeper observation is required to take full advantage of the unprecedented spatial resolution available with Chandra, which appears to be crucial in studying the Fe emission and making progress on important issues in supernova physics such as asymmetries, nucleosynthesis and the location of the mass cut.

We wish to thank Larry Rudnick and Tracey Delaney for communication of their results prior to publication, and for allowing us access to their second epoch Chandra/ACIS data of Cas A prior to becoming public. JML was supported by basic research funds of the Office of Naval Research.

REFERENCES

- Akiyama, S., Wheeler, J. C., Meier, D. L., & Lichenstadt, I. 2003, *ApJ*, 584, 954
- Allende Prieto, C., Lambert, D. L., & Asplund, M. 2001, *ApJ*, 556, L63
- Allende Prieto, C., Lambert, D. L., & Asplund, M. 2002, *ApJ*, 573, L137
- Anders, E., & Grevesse, N. 1989, *Geochim. Cosmochim. Acta*, 53, 197
- Arnett, D. 1996, *Supernovae and Nucleosynthesis*, (Princeton: Princeton University Press)
- Blondin, J. M., Borkowski, K. J., & Reynolds, S. P. 2001, *ApJ*, 557, 782
- Blondin, J. M., Mezzacappa, A., & DeMarino, C. 2002, *astro-ph/0210634*
- Clayton, D. D., Meyer, B. S., The, L.-S., & El Eid, M. F. 2002, *ApJ*, 578, L83
- DeLaney, T. A., & Rudnick, L. 2003, *ApJ*, 589, 818
- Gotthelf, E. V., Koralesky, B., Rudnick, L., Jones, T. W., Hwang, U., & Petre, R. 2001, *ApJ*552, L39
- Grevesse, N., & Sauval, A. J. 1998, *Space Science Reviews*, 85, 161
- Fesen, R. A. *ApJS*, 133, 161
- Fesen, R. A., Becker, R. H., & Goodrich, R. W. 1988, *ApJL*, 329, L89
- Fryer, C. L., & Heger, A. 2000, *ApJ*, 541, 1033
- Fryer, C. L., & Warren, M. S. 2002, *ApJ*, 574, L65
- Fryer, C. L., & Warren, M. S. 2003, in preparation
- Hughes, J. P., Rakowski, C. E., Burrows, D. N., & Slane, P. O. 2000, *ApJ*, 528, L109
- Hwang, U., Holt, S. S., & Petre, R. 2000 *ApJ*, 537, L119
- Iyudin, A. F., et al. 1994, *A&A*, 284, L1
- Iyudin, A. F., Diehl, R.1, Lichti, G. G., et al. 1997, *ESA SP-382*, 37
- Khokhlov, A., M., Höflich, P. A., Oran, E. S., Wheeler, J. C., Wang, L., & Chtchelkanova, A. Yu 1999, *ApJ*, 524, 107L
- Kifonidis, K., Plewa, T., Janka, H.-T., & Müller, E. 2000, *ApJ*, 531, L123

- Kifonidis, K., Plewa, T., Janka, H.-T., & Müller, E. 2003, *A&A*, submitted, astro-ph/0302239
- Klein, R. I., McKee, C. F., & Colella, P. 1994, *ApJ*, 420, 213
- Klein, R. I., Budil, K. S., Perry, T. S., & Bach, D. R. 2003, *ApJ*, 583, 245
- Laming, J. M. 2001a, *ApJ*, 546, 1149
- Laming, J. M. 2001b, *ApJ*, 563, 828
- Laming, J. M., & Hwang, U. 2003, *ApJ*, submitted (Paper I)
- Li, H., McCray, R., Sunyaev, R. A. 1993, *ApJ*, 419, 824
- McKee, C. F., & Cowie, L. L. 1975, *ApJ*, 195, 715
- Nagataki, S., Hashimoto, M., Sato, K., Yamada, S., & Mochizuki, Y. 1998, *ApJ*, 492, L45
- Pinto, P. A., & Woosley, S. E. 1988, *Nature*, 333, 534
- Poludnenko, A. Y., Frank, A., & Blackman, E. G. 2001, *ApJ*, 576, 832
- Silver, E., et al. 2001, in *AIP Conf. Proc.* 587, *Gamma Ray Astrophysics*, ed. S. Ritz, N. Gehrels, & C. R. Shrader (Melville, NY:AIP), 860
- The, L.-S., Clayton, D. D., Jin, L., & Meyer, B. S. 1998, *ApJ*, 504, 500
- Thielemann, F.-K., Nomoto, K., & Hashimoto, M. 1996, *ApJ*, 460, 408
- Timmes, F. X., Woosley, S. E., Hartmann, D. H., & Hoffman, R. D. 1996, *ApJ*, 464, 332
- Truelove, J. K., & McKee, C. F. 1999, *ApJS*, 120, 299
- Vink, J., Kaastra, J. S., & Bleeker, J. A. M. 1996, *A&A*, 307, L41
- Vink, J., Laming, J. M., Kaastra, J. S., Bleeker, J. A. M., Bloemen, H., & Oberlack, U. 2001, *ApJ*, 560, L79
- Vink, J., & Laming, J. M. 2003, *ApJ*, 584, 758
- Wang, C.-Y., & Chevalier, R. A. 2001, *ApJ*, 549, 1119
- Willingale, R., Bleeker, J. A. M., van der Heyden, K. J & Kaastra, J. S. 2002, *A&A*, 381, 1039

Woosley, S. E., & Hoffman, R. D. 1991, *ApJ*, 368, L31

Woosely, S. E., & Weaver, T. A. 1995, *ApJS*, 101, 181

Table 1. Fits to Fe-rich Knots

Knot: ^a	A10	A11	A12	A13	A14	A15	A16	A17
Abundances relative to O, standard background								
$k_B T_e^b$ (keV)	2.11	2.13	1.57	2.03	1.79	1.58	1.98	1.99
net ($10^{11} \text{ cm}^{-3}\text{s}$)	1.80-2.52	1.76-2.59	1.50-1.67	1.40-2.45	1.58-2.07	1.46-1.87	1.71-2.26	1.86-2.25
Mg/O	1.98	2.32	7.92	0.92	2.28	2.19	0.97	1.63
Si/O ^c	1.48-3.07	1.45-3.21	4.98-11.7	8.63e+10-1.90	1.65-3.72	1.74-2.90	7.57e+10-1.15	1.58-2.05
S/O	0.007	0.075	0	0.085	0	0.043	0.018	0.013
Ca/O	< 0.20	< 0.13	< 0.20	0.056-0.15	< 0.075	0.023-0.095	< 0.049	< 0.049
Fe/O	0.40	0.29	1.34	0.38	0.32	0.13	0.14	0.076
N_H (10^{22} cm^{-2})	0.29-0.85	0.23-0.57	0.59-2.48	0.26-0.48	0.22-0.49	0.094-0.19	0.12-0.18	0.066-0.084
EM (10^{11} cm^{-5})	0.43	0.30	0.97	0.34	0.28	0.17	0.14	0.072
χ^2	0.30-0.91	0.22-0.46	0.44-3.20	0.26-0.39	0.18-0.40	0.12-0.20	0.11-0.17	0.051-0.093
χ^2/dof	0.64	0.53	2.41	0.49	0.70	0.50	0.48	0
# dof	0.21-1.07	0.27-0.68	1.50-3.11	0.11-0.85	0.28-1.13	0.18-0.83	0.16-0.79	< 0.074
# cts	1.29	0.72	2.67	0.28	1.09	0.25	0.25	0.26
	0.84-3.20	0.50-1.83	1.30-20.4	0.14-0.35	0.74-1.98	0.17-0.44	0.20-0.34	0.22-0.29
	1.33	1.27	1.37	1.16	1.42	1.17	1.20	1.18
	1.19-1.39	1.17-1.40	1.33-1.40	1.05-1.20	1.35-1.48	1.03-1.38	1.12-1.29	1.05-1.26
	2.25	4.68	1.69	3.23	2.88	4.39	4.26	6.86
	116.4	218.2	180.0	157.3	129.9	78.2	135.1	146.7
	1.25	1.93	1.70	1.69	1.44	0.98	1.54	1.47
	93	113	106	93	90	80	88	100
	5221	6748	5541	4679	5123	3702	4396	5416
Abundances relative to Si, standard background								
$k_B T_e^b$ (keV)	1.73	1.59	1.56	1.23	1.50	1.32	1.20	1.47
net ($10^{11} \text{ cm}^{-3}\text{s}$)	1.65-1.84		1.48-1.61		1.42-1.57	1.32-1.40		
Fe/Si	3.69	7.55	10.1	4.56	5.59	10.9	9.57	7.61
N_H (10^{22} cm^{-2})	3.41-5.48		>7.73		4.12-8.27	5.89-16.4		
χ^2	3.55	2.84	1.91	1.43	3.67	2.25	2.10	3.85
χ^2/dof	3.05-3.74		1.54-2.19		3.30-4.10	1.95-2.83		
# dof	1.44	1.53	1.41	1.66	1.53	1.49	1.50	1.48
	1.35-1.49		1.36-1.49	1.50-1.60	1.33-1.60			
	124.0	236.3	182.2	227.2	145.5	134.8	236.6	243.4
	1.32	2.07	1.70	2.42	1.60	1.66	2.66	2.41
	94	114	107	94	91	81	89	101
Abundances relative to Si, local background								
$k_B T_e^b$ (keV)	1.77	1.68	1.58	1.24	1.52	1.34	1.20	1.47
net ($10^{11} \text{ cm}^{-3}\text{s}$)	1.63-1.95	1.60-1.78	1.52-1.69	1.07-1.92	1.46-1.62	1.29-1.36		
Fe/Si	3.65	7.40	1.02e+12	3.41	5.33	8.33	9.58	7.97
N_H	2.83-5.26	5.30-10.0	>6.85	1.60-5.58	3.75-6.80	6.18-14.7		
	3.84	2.76	1.95	0.39	3.93	2.57	2.10	3.89
	3.27-4.38	2.32-3.38	1.52-2.28	0.28-0.49	3.50-4.58	1.66-2.97		
	1.44	1.45	1.42	0.93	1.54	1.53	1.50	1.48

Table 1—Continued

Knot: ^a	A10	A11	A12	A13	A14	A15	A16	A17
(10^{22} cm ⁻²)	1.33-1.50	1.34-1.52	1.38-1.49	0.69-1.23	1.47-1.60	1.35-1.54		
χ^2	109.4	218.1	170.6	179.3	124.8	111.2	210.3	209.1
χ^2/dof	1.16	1.91	1.59	1.91	1.37	1.37	2.36	2.07
# dof	94	114	107	94	91	81	89	101

^aKnots are numbered moving out to the limb, continuing the east radial series in Paper I. Errors quoted are 90% confidence when the $\chi^2/dof < 2.0$.

^bElectron temperature in keV. Uncertainties are typically ± 0.1 keV.

^cElement abundance ratio by number relative to solar values of Anders & Grevesse (1989): O/H = $8.51e-4$, Mg/H= $3.80e-5$, Si= $3.55e-5$, S= $1.62e-5$, Ar= $3.63e-6$, Ca= $2.29e-6$, Fe= $4.68e-5$, Ni= $1.78e-6$. Note that these are superseded by Grevesse & Sauval (1998), Allende Prieto, Lambert, & Asplund (2001), and Allende Prieto, Lambert, & Asplund (2002). In particular abundances relative to O increase by 1.75. Where abundances are given relative to a particular element, such as O or Si, the abundance of that element was fixed at its solar value for the fits.

Table 2. Fits to Diffuse Regions

Region:	c6a	c6a (joint)	East
$k_B T_e^a$	2.06	1.90	2.59
(keV)	1.88-2.30	1.80-1.97	2.09-2.97
$n_e t_{Si}$	0.74	0.80	1.59
($10^{11} \text{ cm}^{-3}\text{s}$)	0.187-1.71	0.421-1.30	1.26-2.32
S/Si ^b	0	0	0.72
	0.55-0.90
Ar/Si	0	0	2.15
	1.16-3.16
Fe/Si	22.8	20.0	5.77
	16.1-49.4	14.1-27.1	5.43-6.78
$n_e t_{Fe}$	3.3	3.81	...
($10^{11} \text{ cm}^{-3}\text{s}$)	2.5-4.0	3.32-4.90	...
N_H	1.34	1.41	1.27
(10^{22} cm^{-2})	1.27-1.43	1.35-1.47	1.23-1.31
EM (cm^{-5})	1.54e+10	1.89e+10	1.60e+11
χ^2	110.3	262.7	244.8
χ^2/dof	1.33	1.45	1.56
# dof	83	181	157
# cnts ^c	5668 (60%)	5773+5608 (60%)	27816 (57%)
Region Size			

^aElectron temperature in keV. Uncertainties are typically ± 0.1 keV.

^bAbundance by number relative to Si, which is fixed at the solar value.

^cQuantity in parentheses is the fraction of the counts remaining after background subtraction.

Table 3. Ejecta knot abundances and mass coordinates

Region	$q_{\text{OSiFe}}^{\text{a}}$	$q_{\text{FeSi}}^{\text{b}}$	Fe masses ^c	Obs. n_e^{d}	Model n_e^{e}
A10	0.32-0.37	0.35-0.39	7e-5	12	12-20
A11	0.32-0.37	0.39-0.44	8e-5	13	20-39
A12	0.38-0.44	> 0.41	9e-5	15	> 26
A13	0.29-0.34	0.31-0.38	4e-5	7	7-18
A14	0.31-0.36	0.37-0.41	8e-5	12	16-26
A15	0.31-0.34	0.40-0.46	4e-5	7	23-50
c6a	-	0.36-0.38	2e-4	8	14-18
East	-	0.31-0.34	$\sim 1\text{e-}3$	2	7-11

^aEjecta mass coordinate for OSiFe composition, assuming no over/under density.

^bEjecta mass coordinate for FeSi composition, assuming no over/under density.

^cFe masses computed from fitted emission measures and Fe abundances assuming pure Fe, and spherical knots of 1.75'' radius, except for c6a (3.8'' \times 8.8'' box) and East (11'' \times 24'').

^dElectron densities in cm^{-3} from emission measure and fitted abundances.

^eElectron densities in cm^{-3} from $n = 7$ model corresponding to the range in q_{FeSi} .

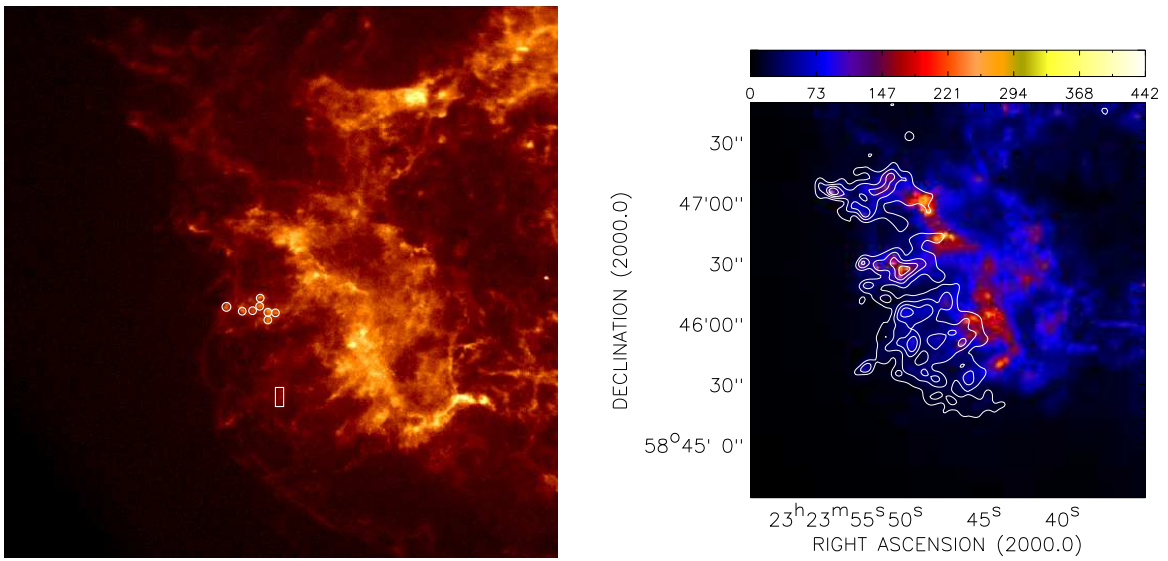


Fig. 1.— Detail of the southeastern region of Cas A as imaged by the Chandra X-ray Observatory in January 2000. The spectral extraction regions used for the linear series of compact Fe-rich knots (circles, starting from the center moving outwards) and the extremely Fe-rich cloud (box) are marked. On the right is the Chandra image of roughly the same region, but including only the photons in the Fe L energy range; superposed are contours showing Fe L line-to-continuum ratios.

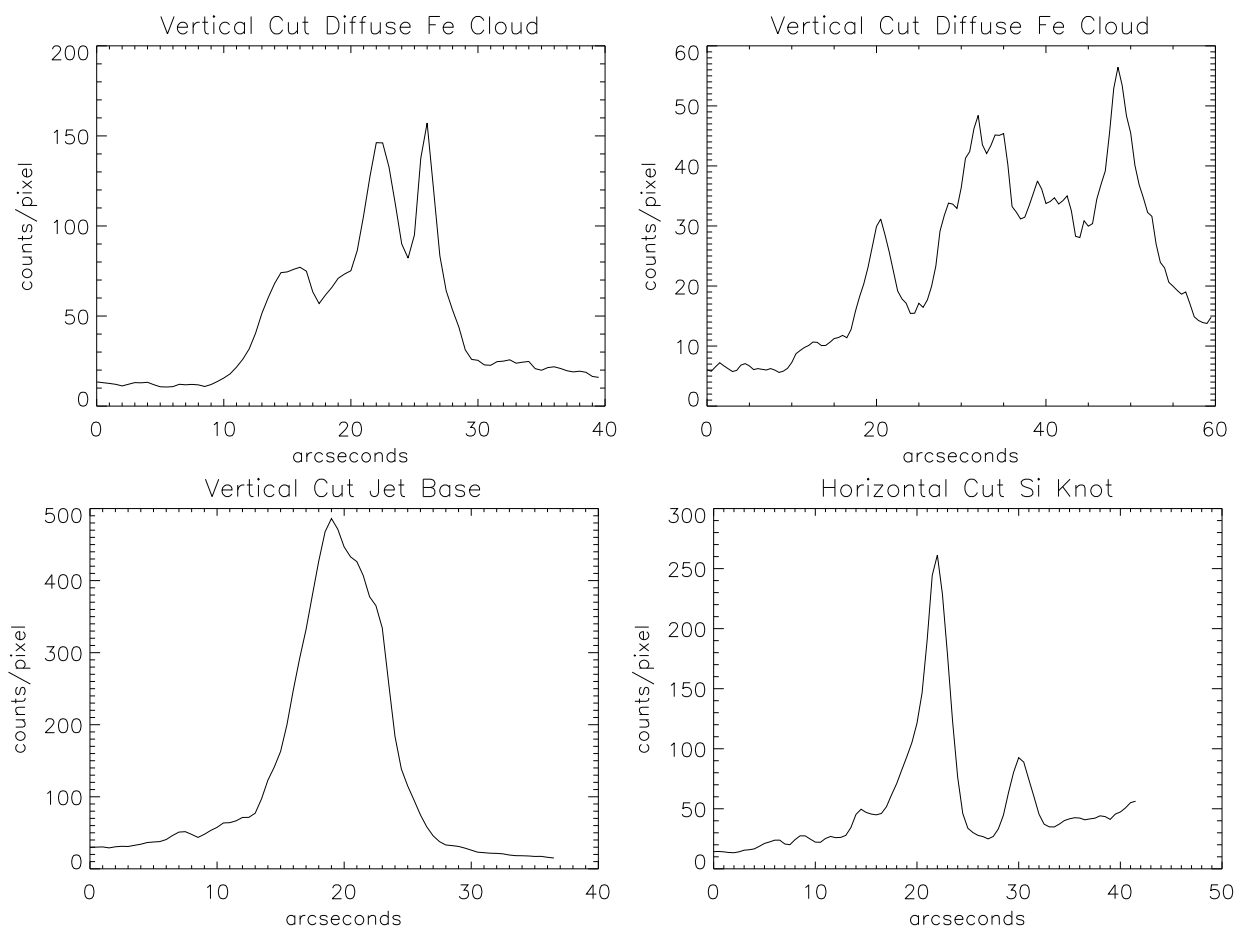


Fig. 2.— Crosswise cuts across various features show the relative surface brightness contrast. Plotted are the average counts per pixel across (a) a $3''$ -wide vertical strip through Fe-rich knots 13 and 14 (b) a $4''$ -wide vertical strip passing through the very Fe-rich diffuse cloud (c) a $6''$ -wide vertical strip through the base of the jet, analyzed in Paper I (d) a $3''$ -wide horizontal strip through an isolated Si-rich knot.

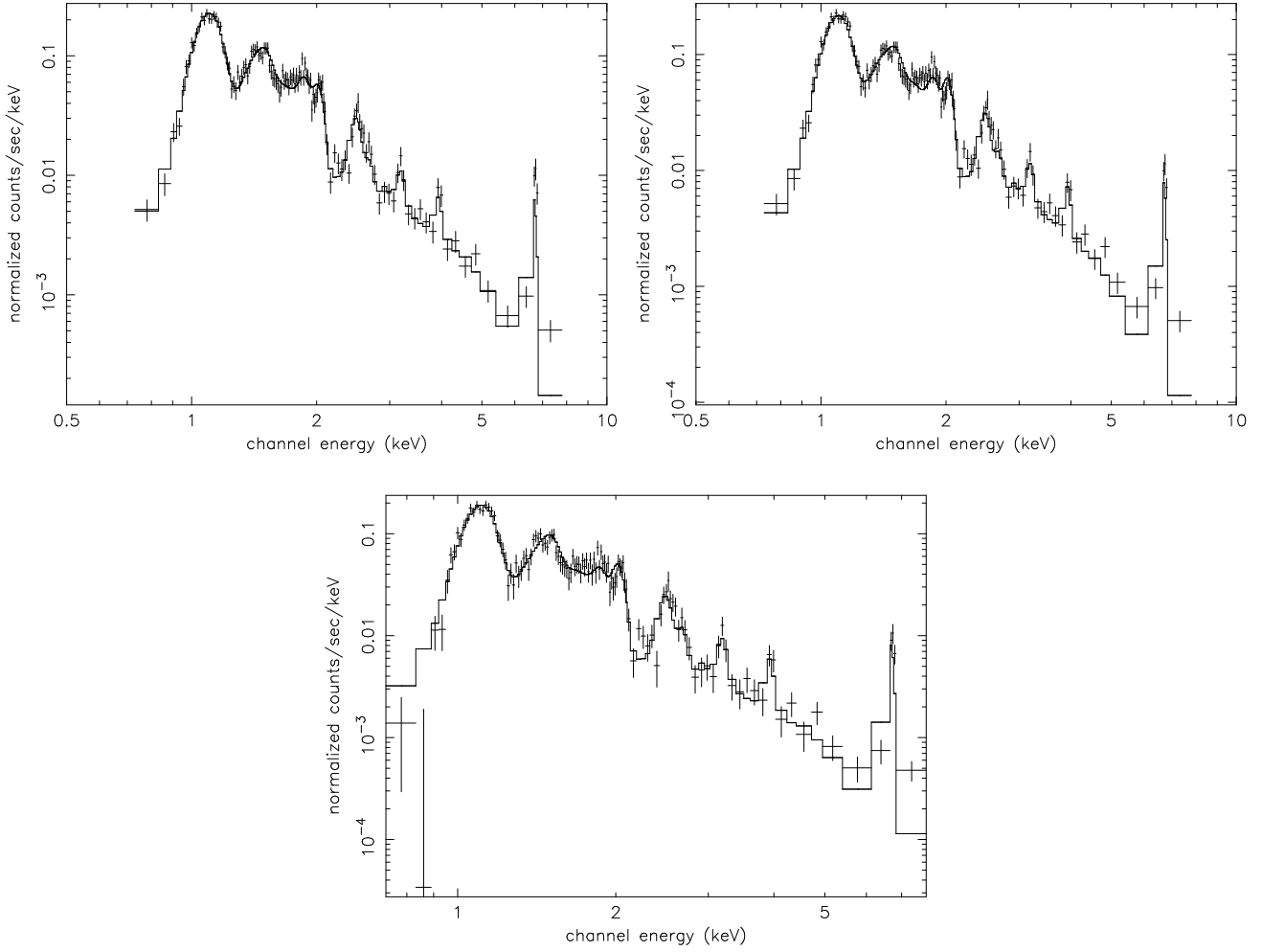


Fig. 3.— Chandra ACIS spectra of a representative Fe-rich knot in the eastern radial series, fitted with a single temperature, single ionization age model with O continuum (left) and Si continuum (right) and the standard off-source background spectrum. In the lower panel, the same knot is fitted with a Si continuum model with a local background.

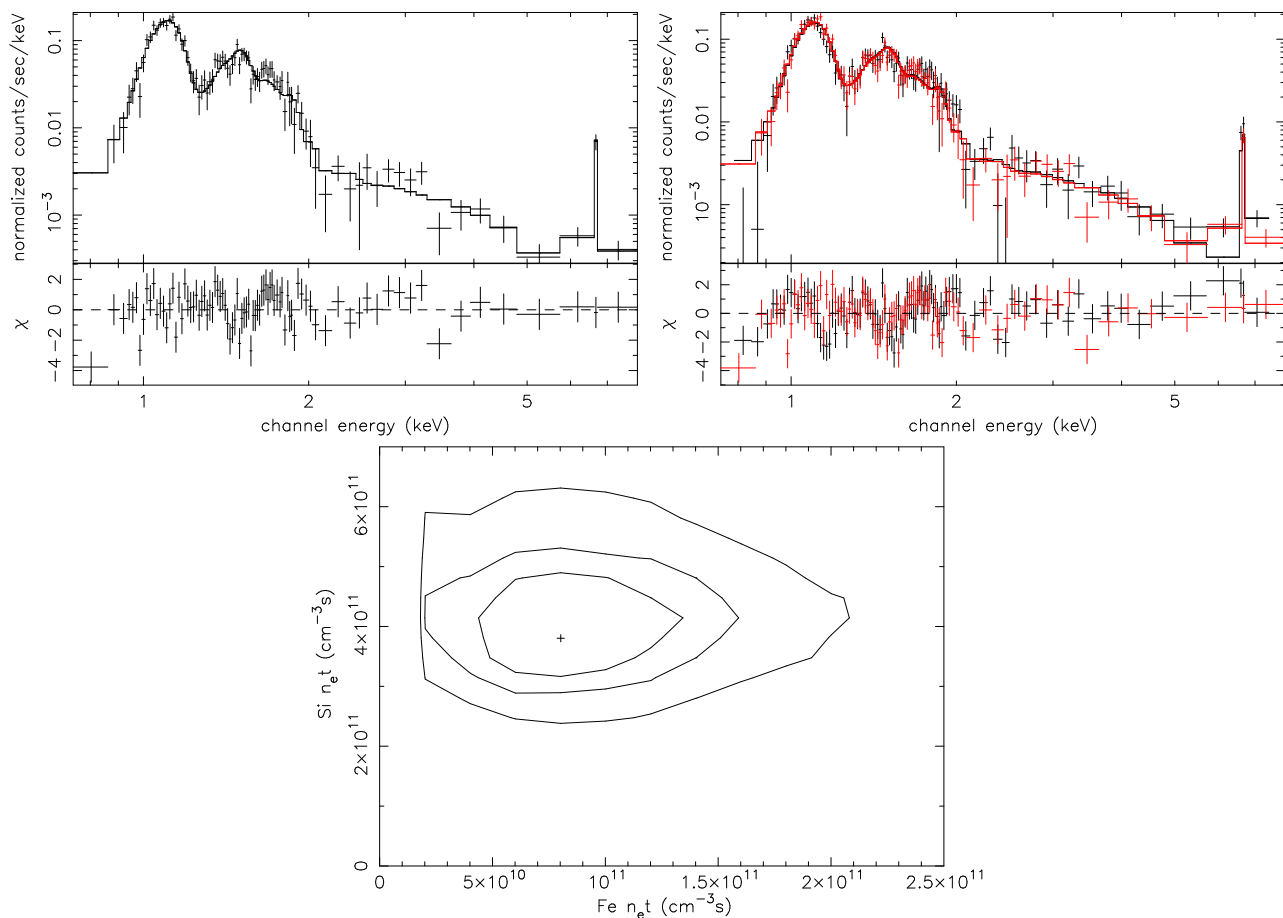


Fig. 4.— (Upper) The 2000 epoch ACIS spectrum of the diffuse Fe cloud is shown with a single temperature model with separate ionization ages for Si compared to Fe and Ni (no other elements are included) in the left panel; the jointly fitted 2000 (red) and 2002 (black) epoch spectra for the Fe cloud are shown in the right panel. (Lower) Confidence contours for Si and Fe ionization ages showing $\Delta\chi^2=2.3,4.6,9.2$ for the joint fit shown above.

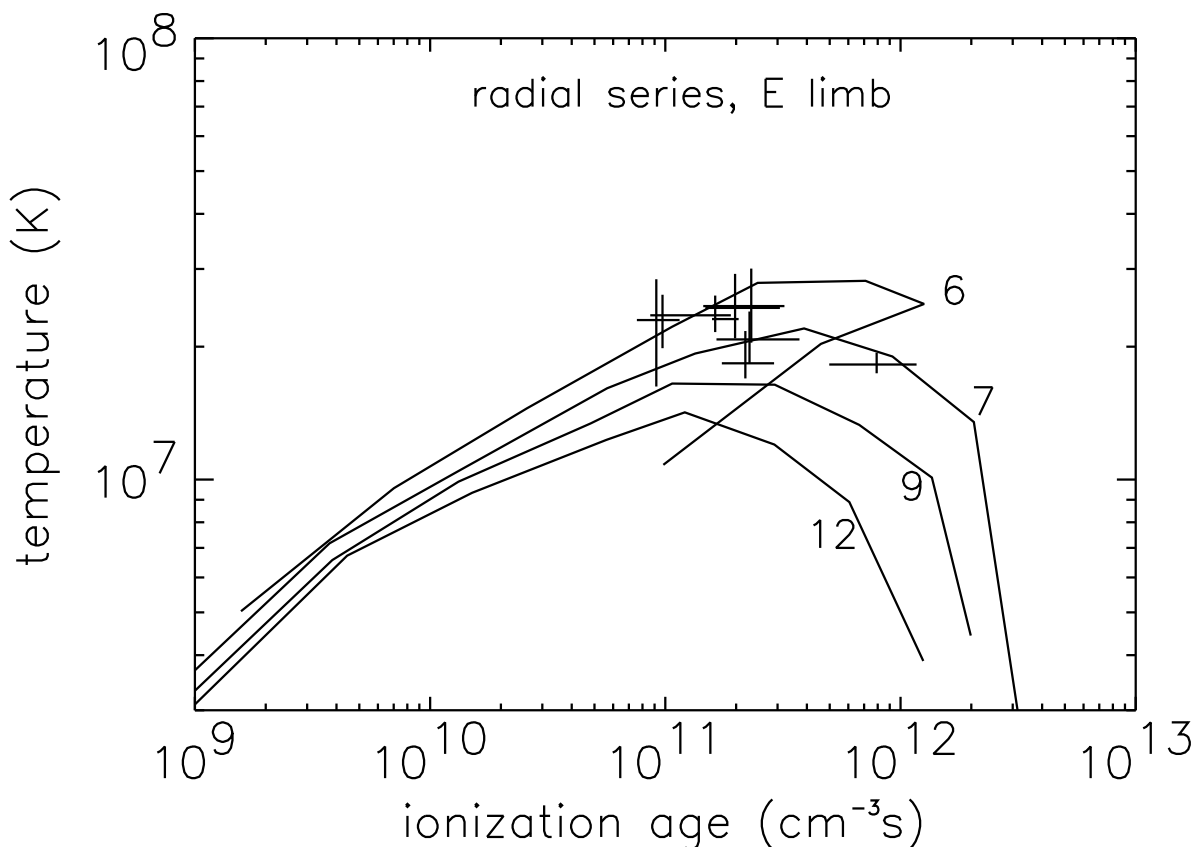


Fig. 5.— Plots of T_e against $n_e t$ for varying ejecta envelope power-law slopes, for a composition O:Si:Fe of 0.83:0.06:0.11 by mass. Data points from the fits to the “A” series of knots are plotted as crosses, with the size of the cross indicating the fit uncertainties. The point at highest $n_e t$ for $n = 6$ corresponds to ejecta at the core-envelope boundary. For higher values of n this plasma undergoes thermal instability.

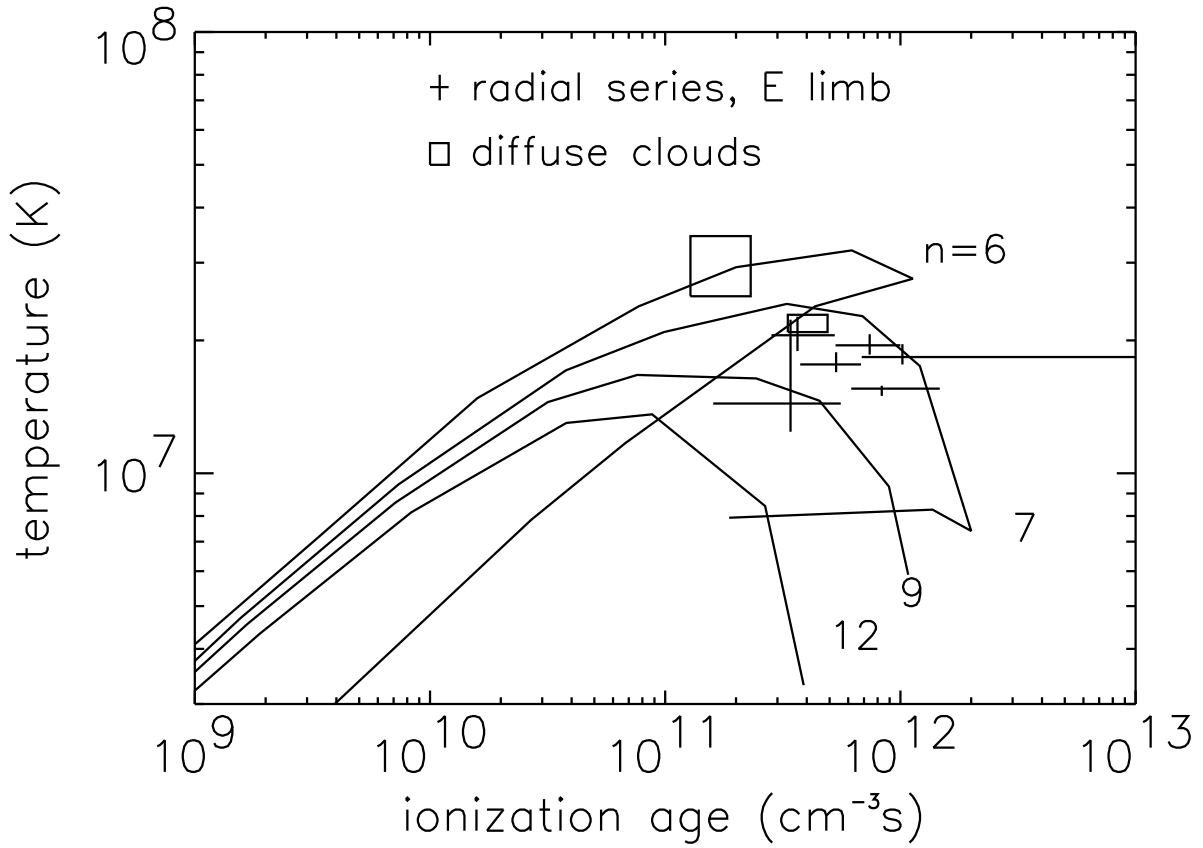


Fig. 6.— Plots of T_e against $n_e t$ for varying ejecta envelope power-law slopes, for a composition Si:Fe of 0.1:0.9 by mass. Data points from the fits to the “A” series of knots are plotted as crosses, with the size of the cross indicating the fit uncertainties. The “diffuse Fe clouds” are plotted as boxes, again with size indicating uncertainties.